ACS APPLIED ELECTRONIC MATERIALS

pubs.acs.org/acsaelm Article

Study of Direct Tunneling and Dielectric Breakdown in Molecular Beam Epitaxial Hexagonal Boron Nitride Monolayers Using Metal–Insulator–Metal Devices

Zhenjun Cui, Yanwei He, Hao Tian, Alireza Khanaki, Long Xu, Wenhao Shi, and Jianlin Liu*

Cite This: *ACS Appl. Electron. Mater.* 2020, 2, 747–755 Read Online

ACCESS | Metrics & More | Article Recommendations | Supporting Information

ABSTRACT: Direct tunneling and dielectric breakdown in molecular beam epitaxial hexagonal boron nitride (h-BN) monolayers were studied based on Ni/h-BN/Ni metal–insulator–metal (MIM) device structures. Effective tunneling areas are orders of magnitude smaller than physical areas of the devices. Statistical Weibull analysis of the breakdown characteristics shows that the breakdown area-scaling law applies to effective areas rather than physical areas of the devices. The h-BN monolayer MIM devices can sustain repeated dc voltage sweeping stresses up to 85 times under an extremely high compliance current of 100 mA, and the critical electric field is determined to be at least 11.8 MV/cm, demonstrating high dielectric strength and reliability of these h-BN monolayers. The mechanism of breakdown and recovery of the h-BN monolayer MIM devices is also discussed.

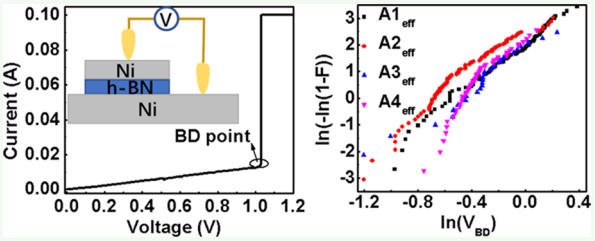

KEYWORDS: *2D materials, monolayer, h-BN, MIM, direct tunneling, dielectric breakdown, soft breakdown*

1. INTRODUCTION

Two-dimensional (2D) materials have attracted tremendous attention recently. Among all 2D materials, 2D hexagonal boron nitride (h-BN) is unique.[1] It has a wide band gap, strong in-plane bonding, superior thermal and chemical stabilities, and excellent dielectric properties. These remarkable properties define 2D h-BN as an ideal dielectric material to gate, encapsulate, or insulate other 2D materials toward novel nanoelectronic devices that possess unparalleled high performance over state-of-the-art counterparts based on three-dimensional materials. For example, in contrast to SiO_2 or other high-k metal oxide dielectric films, h-BN being free of dangling bonds and surface charge traps can effectively reduce carrier scattering rates, and thus increase the field-effect mobility in graphene and other 2D material transistors.[2]

Previously, enormous efforts were spent on the studies of electrical and dielectric properties of SiO_2 and other high-k materials to enhance the performance of metal–oxide–semiconductor field effect transistors in Si digital integrated circuits. For example, in the breakdown (BD) and reliability studies,[3−7] a percolation model was proposed to explain the BD phenomena of those relatively thick insulators, in which randomly distributed defects are created under electrical stress; further accumulation of these defects leads to the formation of defective conductive filaments through the insulators. Likewise, to realize the full potential of 2D h-BN as a dielectric in 2D material electronic devices, it is crucial to study its electrical properties, including electron tunneling and dielectric BD properties.

Toward this end, the first step is to obtain a 2D h-BN single layer and a few layers. Mechanical exfoliation has produced a great deal of 2D h-BN layers from h-BN bulk crystals, which are synthesized by a high-temperature high-pressure process.[8] In the last few years, a great deal of work was devoted to performing direct epitaxy of these films using various techniques, including chemical vapor deposition (CVD),[9−17] molecular beam epitaxy (MBE),[18−26] and sputtering.[27,28] These methods have both advantages and disadvantages in terms of 2D material epitaxy, and some of the comparisons are provided elsewhere.[19−21] As the epitaxial processes of 2D materials become mature quickly, more and more 2D h-BN layers will be controllably produced. The second step is to fabricate a suitable device based on these 2D h-BN layers. A straightforward type of device for this purpose is a metal–insulator–metal (MIM) configuration. To date, several reports have been published to study the electrical transport and BD properties of MIM structures based on 2D h-BN films.[29−39] Among these studies, many relied on the conductive atomic force microscopy technique to extract electrical properties.[29−33] While this method is quite effective, the contact area cannot be precisely determined, leading to a limited

Received: December 12, 2019
Accepted: March 3, 2020
Published: March 3, 2020

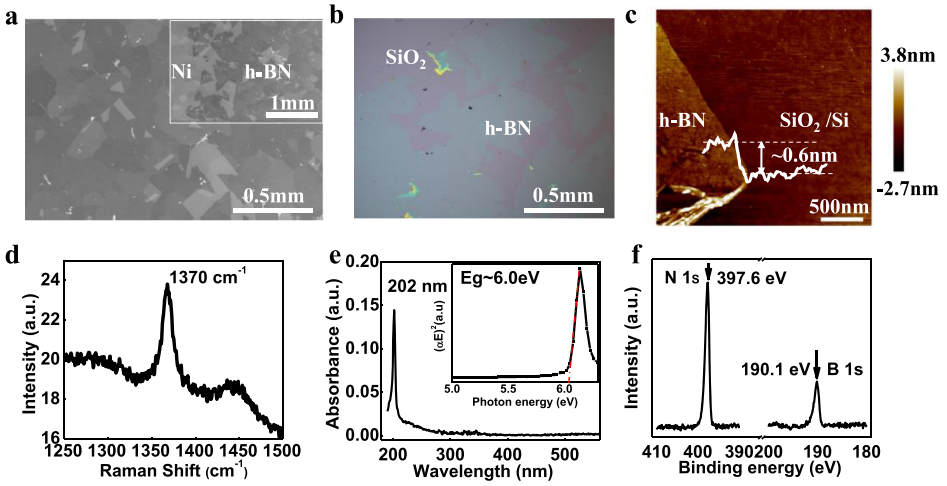

Figure 1. Characterization of the h-BN monolayer (Sample 1). (a) SEM image of the sample, showing a continuous h-BN film on a Ni substrate; the inset displays the edge area of the film, where some discrete h-BN flakes and Ni substrate are seen. (b) OM image of transferred h-BN on a SiO_2-coated Si substrate. (c) AFM image of the transferred h-BN film near an edge of the film. The inset shows a scanning profile across the sample edge, showing a step height of about 0.6 nm. (d) Raman spectrum of the transferred h-BN on SiO_2-coated Si, showing a characteristic E_{2g} phonon peak at 1370 cm^{-1}. (e) Absorption spectrum of the h-BN film transferred onto a sapphire substrate. The inset shows the Tauc plot determining the bandgap of h-BN to be about 6.0 eV. (f) XPS spectrum of B 1s and N 1s signals at 190.1 and 397.6 eV, respectively.

understanding of electron tunneling through the h-BN barriers. Although some other reports have adopted MIM devices using direct metal or graphene contacts,[28,34−39] most are based on thicker h-BN films of a few layers to a few tens of layers. Thus, limited understanding remains for the electrical and dielectric properties of ultimately thin h-BN single layers. Moreover, no device area-dependent electrical property and thorough reliability studies have been reported in these MIM devices based on single-layer h-BN, which are important to reveal the fundamental mechanisms behind the electron tunneling and BD of these films.

In this paper, we report our comprehensive electrical property studies of h-BN monolayers. These h-BN monolayers were grown on Ni (100) substrates by MBE. Ni/h-BN/Ni MIM devices with various device areas were fabricated. By measuring currents under different ways of voltage stress, followed by statistical data analysis including the Weibull distribution, we have demonstrated local hot-spot tunneling, high critical electric field, high endurance, and high dielectric strength of these h-BN monolayers. In addition, we have discussed the mechanism of device BD and recovery.

2. METHODS

Ni (100) foils from Alfa Aesar of 0.1 mm thickness and 99.995% purity were polished using an SBT 920 Lapping and Polishing workstation. Detailed preparation procedures were reported elsewhere,[23] which led to a smooth substrate surface with a root mean square roughness of less than 1 nm. They were cut into pieces of 1 cm × 1 cm as substrates. The pieces were degreased and deoxidized with acetone, IPA, and diluted hydrochloric acid (10%), followed by rinsing with deionized water and blow-drying with nitrogen. The substrates were immediately loaded into a modified Perkin Elmer 425B MBE system with a background pressure of ~10^{-9} Torr maintained by a turbomolecular pump.

Three samples with slightly different growth conditions were grown. The substrates were heated to the growth temperature and annealed at this temperature under a 10 sccm flow of hydrogen gas for a period of time. Then, 0.5 sccm of C_2H_2 gas was introduced into the chamber to carburize the substrates. Carburization of Ni (100) enhances the growth of h-BN monolayers, which is described in detail elsewhere.[24,39] H-BN films were grown immediately after the carburization process. The h-BN growth was realized by simultaneous introduction of B and N sources onto Ni substrates for a period of time at the growth temperature. A Knudsen effusion cell filled with B_2O_3 powder (Alfa Aesar, 99.999% purity) was used as the boron (B) source. An electron cyclotron resonance (ECR) system was used to generate the nitrogen (N) plasma (Airgas, 99.9999% purity). The ECR current was set to 60 mA with a power of 228 W. High-purity ammonia (American Gas Group, 99.9995%) also served as the N source. After the growth, the samples were cooled down to room temperature at a rate of 10 °C/min. Table S1 summarizes the detailed growth conditions of these samples.

Optical microscopy (OM) images were obtained using a Nikon LV-150 OM system. Scanning electron microscopy (SEM) images were acquired using a FEI NNS450 system. Atomic force microscopy (AFM) images were obtained using a Veeco D5000 AFM system. A Varian Cary 500 spectrometer was used for absorption measurements. A HORIBA LabRAM system equipped with a 60 mW, 532 nm green laser was used for Raman characterization. X-ray photoelectron spectroscopy (XPS) characterization was conducted using a Kratos AXIS ULTRA XPS system equipped with an Al Kα monochromatic X-ray source and a 165 mm mean radius electron energy hemispherical analyzer.

Two-terminal MIM devices based on the h-BN films on Ni (100) were fabricated by using sequential standard photolithography, Ni metal deposition, lift-off, and plasma etching processes. A Ni layer of 100 nm was deposited on the as-grown samples, and subsequently patterned to form square-shaped metal contacts with edge lengths of 25, 50, 100, and 200 μm. Reactive ion etching was performed with a 50 sccm SF_6 plasma, under a power of 600 W for 15 s to etch the h-BN films between devices to ensure isolation of different devices on the same substrate. The Ni substrates were used as global bottom metal contacts for all devices. An Agilent 4155C semiconductor parameter analyzer and a Signatone probe station equipped with probing tips of about 5 μm were used to measure the electrical properties of the Ni/h-BN/Ni devices.

3. RESULTS AND DISCUSSION

Figure 1 summarizes the structural and optical characterization results of Sample 1. Figure 1a shows an SEM image of the center area of Sample 1 and the inset is an SEM image of its edge area. H-BN and Ni substrates appear relatively dark and bright, respectively. From the contrast, it is concluded that the center area of the sample is covered by h-BN, while there are

https://dx.doi.org/10.1021/acsaelm.9b00816
ACS Appl. Electron. Mater. 2020, 2, 747−755

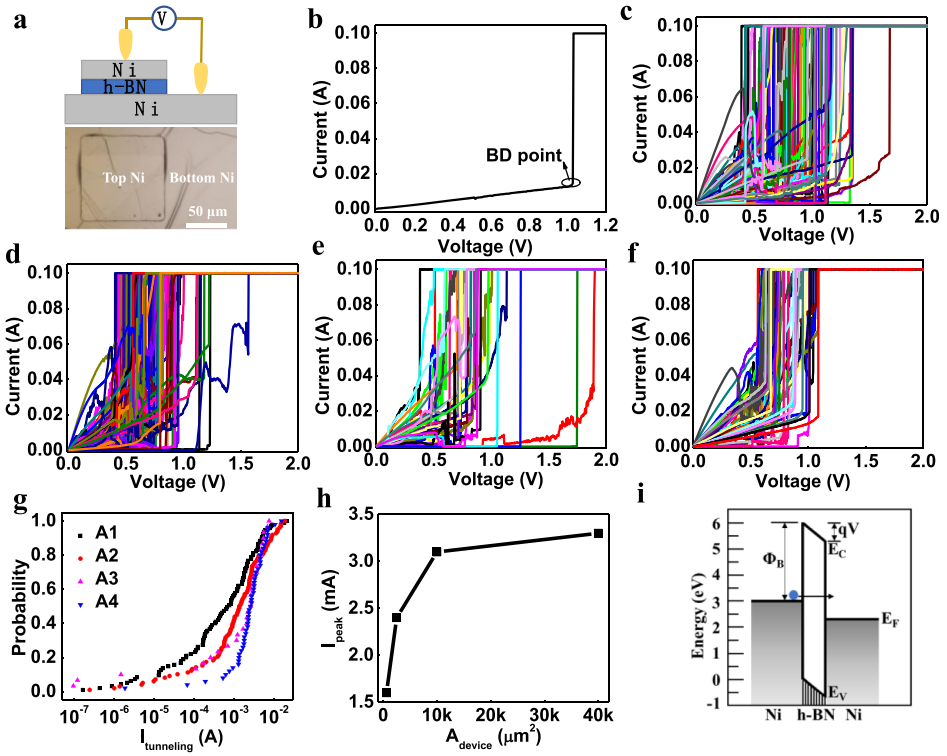

Figure 2. (a) Ni/h-BN/Ni device structure. The top schematic is a cross-sectional view of measurement configuration. Bottom portion shows a bright-field OM image of a device with a 100 × 100 μm^2 top electrode. (b) Typical $I-V$ characteristic of a Ni/h-BN/Ni device with a size of 25 × 25 μm^2 under a compliance current of 100 mA. Dielectric BD at a voltage of ∼1.0 V is demonstrated. (c) $I-V$ curves of 97 devices with an area of 25 × 25 μm^2. (d) $I-V$ curves of 96 devices with an area of 50 × 50 μm^2. (e) $I-V$ curves of 30 devices with an area of 100 × 100 μm^2. (f) $I-V$ curves of 50 devices with an area of 200 × 200 μm^2. (g) The cumulative probability distribution of $I_{tunneling}$ with different device areas. All tunneling currents were collected at a bias of 0.1 V. Black, red, magenta, and blue symbols represent devices with a size of 25 × 25, 50 × 50, 100 × 100, and 200 × 200 μm^2, respectively. (h) The peak tunneling current (I_{peak}) as a function of device area, where I_{peak} is 63% of cumulative current value. Tunneling current being not linearly proportional to the device area is evident. (i) Schematic of the DT mechanism of the Ni/h-BN/Ni device.

Table 1. Summary of Current Ranges and Peak Currents at 0.1 V and Parameters of Area-Dependent BD Voltage Distributions as a Result of Gaussian Fitting and Weibull Analysis of Ni/H-BN/Ni Devices (A1−A4), Where n Represents the Number of Samples and R^2 is the Coefficient of Determination

device	A1	A2	A3	A4
A_{device} [μm^2]	25 × 25	50 × 50	100 × 100	200 × 200
n	97	96	30	50
$I_{tunneling}$ range [mA]	1.7 × 10^{-3}−21	2.5 × 10^{-4}−19	9.6 × 10^{-5}−8	1.9 × 10^{-3}−1.5
I_{peak} [mA]	1.6	2.4	3.1	3.3
$A_{effective}$ [μm^2]	0.148	0.221	0.286	0.304
V_{BD} range [V]	0.47−1.10	0.30−1.60	0.30−1.70	0.47−1.10
peak V_{BD} (Gauss) [V]	0.90	0.68	0.75	0.67
R^2 (Gauss)	0.74	0.90	0.83	0.88
α_F [V]	1.00	0.72	0.79	0.73
$\alpha_{Weibull}$ [V]	0.97	0.74	0.84	0.78
β	3.87	3.98	3.69	3.36/9.34
R^2 (Weibull)	0.99	0.95	0.94	0.91

discrete h-BN flakes near the edge area. Figure 1b shows an OM image of transferred Sample 1 on a SiO_2-coated Si substrate. The detailed transfer process using $FeCl_3$ solution is reported elsewhere.[39] As seen from Figure 1b, while the continuous film was partially broken during the transfer process, a large-area h-BN film is preserved. Figure 1c shows an AFM image of the transferred Sample 1. The inset shows a scanning profile across an edge of the transferred film, indicating a thickness of ∼0.6 nm. With the consideration of the AFM tip effect,[40] this thickness suggests that the film is a monolayer. Figure 1d shows the Raman spectrum of the transferred Sample 1. A characteristic E_{2g} phonon peak is found at 1370 cm^{-1}, implying that the film is a single layer.[41] Figure 1e shows an absorption spectrum of transferred Sample 1 on a sapphire substrate. A peak at 203 nm with a sharp absorption edge is observed. The inset shows its Tauc plot, assuming a direct semiconductor. A bandgap of 6.0 eV is determined, which matches that of h-BN.[42] Figure 1f shows an XPS spectrum of as-grown Sample 1. B 1s and N 1s peaks are at the binding energies of 190.1 and 397.6 eV, respectively.

https://dx.doi.org/10.1021/acsaelm.9b00816
ACS Appl. Electron. Mater. 2020, 2, 747−755

Multi-peak fitting of these peaks is shown in Figure S1 in the Supporting Information, revealing the sp^2 B−N bond phase,[43,44] sp^3 B−N bond phase, and oxygen impurity-related peak.[24,25] No other impurities, for example, the incorporation of C as substitutional impurities in the film are observed in the XPS studies. Further assessment of the intensities of the peaks yields the B and N stoichiometry ratio of unity. Figure S2 shows the characterization results of Samples 2 and 3. Similar to Sample 1, both samples have continuous h-BN monolayers on Ni substrates.

Figure 2a shows a cross-sectional schematic of a Ni/h-BN/Ni device and a bright-field OM image of a device with a size of 100 × 100 μm^2. Figure 2b shows a typical $I-V$ characteristic of a device with a size of 25 × 25 μm^2. The current increases linearly with the increase of the bias, suggesting that the device is operated in a direct tunneling (DT) region under small and moderate voltages.[45,46] As the voltage reaches ∼1 V, dielectric BD occurs, and the current abruptly rises to the compliance current of 0.1 A. The current and voltage read at this point are regarded as the BD current (I_{BD}) and the BD voltage (V_{BD}), respectively. Figure 2c−f shows the $I-V$ family curves of A1−A4 devices of 25 × 25, 50 × 50, 100 × 100, and 200 × 200 μm^2, respectively. Similar characteristics to that of Figure 2b are demonstrated in most devices, while the current bumps of the curves especially in a larger bias region emerge in some devices, which is due to trap-assisted tunneling in these occasions.[47] Figure S3 shows some representative $I-V$ characteristics for clarity. In addition, V_{BD} fluctuates among the devices with the same device area as well as different sizes. V_{BD} distributions are discussed later. Figure 2g shows the cumulative probability of DT currents at a bias of 0.1 V for the devices with all four sizes. Since the tunneling currents span a wide range (summarized in Table 1), the most probable DT currents or peak currents (I_{peak}) at 0.1 V are obtained by setting the cumulative probability at 63.2%. The I_{peak} values for the devices with four sizes are also summarized in Table 1. These currents are comparable with that of the tunneling devices based on CVD-grown[48] and exfoliated[30] h-BN monolayers. Figure 2h shows I_{peak} as a function of device area. Although I_{peak} increases with the increase of the device area, it tends to saturate in larger devices, namely the relationship is surprisingly not linear.

To clarify this intriguing phenomenon, we hypothesize that the electron tunneling occurs only in an effectively local small area (A_{eff}), instead of throughout the entire device area (A_{device}) in these atomic layer tunneling devices, especially with very large A_{device}. To prove this hypothesis, one way is to calculate the tunneling current using the existing model[45,46] and compare the values with the experimental data. Figure 2i shows a schematic of the band-alignment diagram of the MIM tunneling device. Schottky barrier height of Ni/h-BN junction Φ_B is assumed to be 3.0 eV, which is half of the bandgap of h-BN. This value or similar values were also observed between h-BN and other metals.[30,36,49] The barrier width d, namely the thickness of the h-BN monolayer is 0.66 nm, assuming this as the van der Waals distance between the h-BN and top/bottom Ni contacts.[39] Under a small applied bias of 0.1 V, the DT mechanism dominates the electron tunneling process. The DT current is expressed as[45,46]

$$I(V, T) = I(V, 0) \times \left\{1 + \left[\frac{3 \times 10^{-9}(dT)^2}{\Phi_B/q}\right]\right\} \quad (1)$$

where $I(V, 0) = \frac{A_{eff}\sqrt{2m\Phi_B}q^2V}{h^2d}\exp\left(\frac{-4\pi d\sqrt{2m\Phi_B}}{h}\right)$, m is the electron effective mass, which is 0.26 m_0,[50] h is the Planck constant, q is the fundamental charge, and d is expressed in angstroms. $I(V,0)$ is the well-known Simmons DT current for an MIM device at an absolute temperature of 0 K, and the terms in the {} bracket modify $I(V,0)$ to $I(V,T)$, a DT current at a temperature of T, which is 300 K here. Based on the I_{peak} values at 0.1 V, the effective areas A_{eff} for electron tunneling in devices A1−A4 are calculated and summarized in Table 1. The effective areas are found to be orders of magnitude smaller than physical areas of the devices, respectively. This proves that the electron tunneling indeed goes through a surprisingly much smaller local area, namely, electrons do not flow through a great deal of remaining device areas during the operation, which are somewhat inactive. A similar phenomenon was also observed in other tunneling devices, such as $Al/AlO_X/Al$ tunneling junctions[51] and magnetic tunneling junctions.[52] The appearance of these "hot spot" tunneling junctions was explained to be partially due to uneven thickness of the films.[51,52] In our samples, although there are some multi-layered island adlayer structures shown as white features in these SEM images, which shall not carry tunneling currents compared with monolayers due to thicker barriers, the majority of areas have h-BN monolayers because the percentage of occupied areas by these adlayers is very low. Thus, the contribution from the non-uniform film thickness in our devices could be negligible. A much smaller effective area for electron tunneling could originate from the existence of non-uniform gap distances between a single h-BN layer and Ni (both the top contact metal and the bottom Ni substrate). During the h-BN growth at high temperatures, the film may largely conform to the relatively flat surface; nevertheless, when the substrate temperature decreases to room temperature, uneven gaps may be formed due to different expansion coefficients of Ni and h-BN. In addition, since the deposition of Ni onto h-BN to form top metal contact is done at room temperature, those Ni atoms nearest to the h-BN plane may not conform onto the h-BN monolayer with the same distance across the entire surface. Further experiments such as high-resolution transmission electron microscopic technique may be necessary to elucidate the hypothesis.

Figure 3a shows the histogram of BD voltage distribution of devices of four different sizes. Gaussian distribution fittings were performed, and the BD voltage ranges and peak BD voltages are summarized in Table 1. Nevertheless, the coefficients of determination R^2 summarized in the Table are also generally smaller than 0.9. This means that not all the BD voltages can be fitted to the perfect Gaussian distribution. To address this issue, Weibull distribution analysis[53] was performed. The cumulative failure probability F can be calculated from

$$F = \frac{n}{N+1} \quad (2)$$

where n = 1, 2, ..., N is the number of broken-down devices, and N is the total number of the devices. Figure 3b shows cumulative failure probability as a function of BD voltage for all A1−A4 devices. From the plot, the most probable BD voltage or peak voltage α_F, which is defined as the voltage at which 63.2% of devices have broken down, is obtained for A1−A4 devices and summarized in Table 1. These values differ for

https://dx.doi.org/10.1021/acsaelm.9b00816
ACS Appl. Electron. Mater. 2020, 2, 747−755

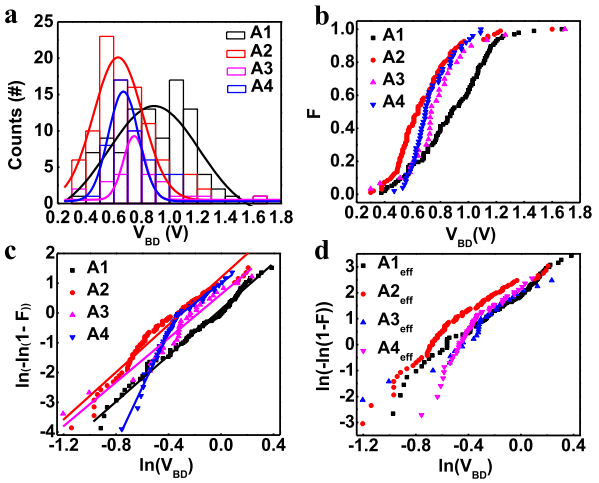

Figure 3. (a) Histogram of BD voltage distribution with a bin size of 0.1 V and relevant Gaussian distribution fittings. (b) Cumulative failure probability F as a function of V_{BD}. (c) Weibull plot of BD voltage distribution. (d) Normalized Weibull plot by scaling effective areas A_{eff} to 1 μm^2. Data overlapping for $A1_{eff}$–$A3_{eff}$ in most of the BD voltage ranges and $A4_{eff}$ in a higher voltage range is acceptable.

different device sizes and are also slightly different from that obtained from Gaussian fitting.

To further clarify the area-dependent BD characteristics and elucidate the BD mechanism, the cumulative failure probability F can be described using the so-called Weibull cumulative distribution function F (V_{BD}), which is defined as (3).

$$F(V_{BD}) = 1 - \exp\left[-\left(\frac{V_{BD}}{\alpha}\right)^{\beta}\right] \quad (3)$$

where α is the most probable BD voltage, which is also referred to as the Weibull scale parameter, and β, the shape parameter, is the Weibull modulus indicating the width of the distribution, which characterizes the degree of V_{BD} variation (uniformity), leading to the determination of the failure mode classification. The Weibull cumulative distribution function can be rearranged by taking two logarithms

$$\ln[-\ln(1 - F)] = \beta \ln(V_{BD}) - \beta \ln \alpha \quad (4)$$

Thus, the Weibull plot of $\ln[-\ln(1 - F)]$ versus $\ln(V_{BD})$ can be used to extract the slope β and α from the y-intercept, $-\beta \ln \alpha$. Assuming the BD goes through the defect, and these defects are randomly distributed across the entire areas of the devices, the BD voltages would follow an area-scaling law[54]

$$\frac{V_{BDm}}{V_{BDn}} = \left[\frac{A_n}{A_m}\right]^{1/\beta} \quad (5)$$

where A_m and A_n are devices with arbitrary sizes. The corresponding area-scaling Weibull plot for devices with different areas is derived as[54]

$$\ln[-\ln(1 - F_m)] - \ln[-\ln(1 - F_n)] = \ln(A_m/A_n) \quad (6)$$

Thus, the Weibull plot data have identical β, and the fitted lines will overlap if scaled by $\ln(A_m/A_n)$.

Figure 3c shows the Weibull plots of A1–A4 devices. The α and β values are summarized in Table 1. It is evident that Weibull plots for A1–A3 devices in the entire BD voltage ranges and for A4 device in the higher BD voltage range have similar β values ($3.36 < \beta < 3.98$), indicating an identical intrinsic BD mechanism through randomly distributed defects.[55] A much larger β value of 9.34 is also extracted for the A4 device in the lower BD voltage range, which suggests the deviation from the intrinsic BD mechanism and the emergence of new BD paths.[56] The α values are very similar to the BD voltages obtained from cumulative failure probability analysis in Figure 3b, suggesting that the two methods are complementary to each other for reliably extracting the peak BD voltages.

Figure 3d shows the normalized Weibull plots after scaling effective areas to a common area of 1 μm^2. Data points for the normalized A1–A3 devices in an almost entire range of BD voltages and normalized A4 devices in the higher voltage range overlap well. Nevertheless, normalized Weibull plots after scaling the physical areas of the devices (A1–A4) to a common area of 1 μm^2 do not overlap (Figure S4 in the Supporting Information). This noticeable difference further demonstrates that the devices operate across only small effective areas rather than entire physical areas of the devices. Furthermore, it implies that the BD locations are randomly distributed. As seen from Table 1, the effective area generally increases with the increase of the physical areas; however, it tends to saturate. For example, as the device area increases from 100 × 100 to 200 × 200 μm^2, the effective area only increases from 0.286 to 0.304 μm^2, namely, about only 6.3%. According to the BD voltage area-scaling law (eq 5), the BD voltage will saturate, as the device area increases. Thus, it is reasonable to designate the minimum BD voltages in all the presently studied devices to be that of the devices of 200 × 200 μm^2, which is ~0.78 V according to Weibull analysis. Accordingly, the minimum effective BD electric field (E_{BD}) can be determined to be 11.8 MV/cm, which is comparable with that of thick high-quality SiO_2.

Figure 4a shows the I–V curves of a Ni/h-BN/Ni device of 50 × 50 μm^2 for 91 successive operations. The compliance current is set to 100 mA for all these operations. As seen from Figure 4a, the 1st to 85th curves display typical I–V

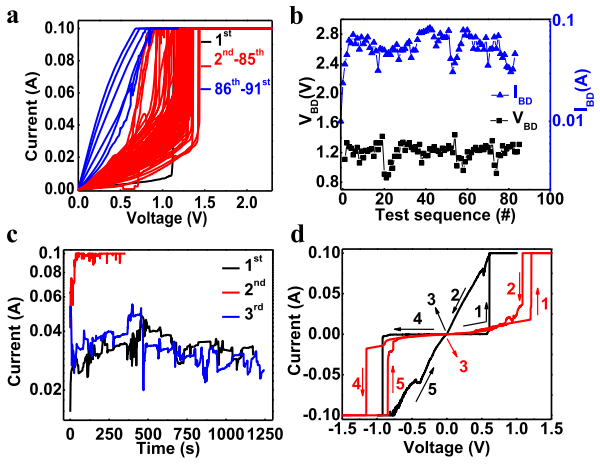

Figure 4. (a) I–V characteristics of a Ni/h-BN/Ni device of 50 × 50 μm^2 for 91 successive operations. (b) Distribution of the BD voltages and BD currents of the device within the first 85-BD cycles. (c) Three successive I–t curves collected with respect to certain constant voltage stresses. (d) I–V characteristics of Ni/h-BN/Ni devices of 50 × 50 μm^2 operated by a sweeping bias, demonstrating two typical self-recovery behaviors.

https://dx.doi.org/10.1021/acsaelm.9b00816
ACS Appl. Electron. Mater. 2020, 2, 747–755

characteristics of a MIM device, namely, the current increases monotonously with the increase of the bias until BD when it sharply increases and reaches the compliance current. The $I-V$ curves from 86th to 91st become linear, and the currents increase sharply and quickly reach the compliance current level, suggesting that the device is totally conductive, thus is physically worn out and cannot be recovered. The reversible and repeatable BD events for the first 85-operations can be regarded as soft BD (SBD), after which physically hard BD (HBD) is reached. The SBD involves the passing of large amounts of currents through conductive paths. This process generates large Joule heat locally, which supplies energy to nearby atoms in both h-BN and adjacent Ni electrodes, leading to lateral BD spot propagation and electromigration. Further repeated SBD operations ultimately create permanent conduction paths and dramatic failure of the device. The fact that the device can endure DC voltage sweep and undergo BD events up to 85 times suggests that the h-BN monolayer is electrically robust.

Figure 4b shows the cumulative distribution diagram of BD voltages and BD currents in the test sequence of the corresponding device. The change in V_{BD} and I_{BD} with the test sequence is random and stochastic. However, BD voltages and BD currents stably center around 1.21 V and 0.056 A, respectively, as the test sequence goes on, indicating high reliability of the device. It is worth mentioning that previously reported SBD behaviors in other dielectric films refer to either abrupt pre-degradation before HBD or BD with a small compliance current.[57] Both scenarios indicate that the SBD I_{BD} values are smaller than that of HBD. Here, the currents going through the h-BN monolayers via recoverable SBD processes are the same as that of the irrecoverable HBD, which are limited by the large compliance current of 100 mA. Thus, the identification of whether the BD is SBD or HBD only depends on the recoverability of the devices. In the literature,[58] BD behaviors with a BD current at a level of only a few mA were already treated as irrecoverable HBD. The fact that the h-BN monolayer devices here do not undergo BD until a BD current of ~60 mA and can further sustain 100 mA compliance currents, and still recover, revealing ultrahigh dielectric strength of h-BN monolayers compared with other dielectric materials.

The successive time dependence of the current ($I-t$) prior to and after SBD events under constant biases was carried out to further understand the BD mechanism and reliability of the Ni/h-BN/Ni devices. Figure 4c shows a typical result of a device with a size of $50 \times 50\ \mu m^2$. The device was firstly biased at 0.5 V; the $I-t$ curve shows abrupt random fluctuations around a current of about 30 mA. The fluctuation is a type of random telegraph noise signal, which is an indication of the trapping and de-trapping of charges in the h-BN monolayer.[32] Then, 0.8 V was applied to the device, at which the current quickly increases to the compliance current, indicating the BD of the device. Lastly, a voltage of 0.5 V was applied to the device again. The $I-t$ curve is very similar to the initial state, which confirms the good self-healing property of the device after SBD at 0.8 V.

The device recovery was further studied by performing voltage sweep operations. Figure 4d shows the $I-V$ characteristics of two complementary recovery results. Both characteristics exhibit polarity independent. Forward sweeps in both polarities ensured the device to undergo SBD events, and the backward sweeps allow the bias to linearly scale back to zero. In one case, as shown in the black curve in Figure 4d, the currents in the backward sweeps almost linearly decrease with the decrease of the bias, and the device completely recovered to the original state once stress is released. The red curve in Figure 4d demonstrates that the currents abruptly drop and the device returns to the original state as the backward voltage reduces but before the bias is totally released, which is a typical threshold resistive switching characteristic. The recovery characteristics demonstrated in both Figure 4a,d may be understood as follows: Epitaxial 2D materials including h-BN and transition metal dichalcogenide materials are found to usually have intrinsically formed defects such as point defects, antisite defects, extended defects, and grain boundaries.[59−61] The present h-BN films shall also have some pre-existing defects such as boron or nitrogen vacancies and grain boundaries. These defects are passivated under thermal equilibrium. The nature of passivation may have something to do with trapping electron or hole charges onto these defects. During the operation of the devices, enormous Joule heat is generated especially at the BD point. The high-temperature change as a result of Joule heating can de-trap these pre-existing defects making them unpassivated and active. In addition, it could dislodge the atoms in the films, leading to additional defects. These defects act as the conductive paths during the BD process. As the applied bias is reduced or relieved, the heat generation becomes less. In the meantime, because both monolayer h-BN[62,63] and Ni[23] have high thermal conductivities, dissipation of the generated heat is efficient. Thus, charges can quickly fill the de-trapped defects because their energy levels usually are deep in the forbidden gap of h-BN, and the film can recover from the SBD state to the original state.[64] Another reason of device recovery can be related to the electric field across the film. The electric field increases with the increase of the bias across the device. As the electric field reaches the critical value at the BD point, these defects are readily unpassivated or detrapped. As the electric field is reduced or relieved, charge carriers re-fill the de-trapped defects, leading to device recovery.

4. CONCLUSIONS

We have demonstrated a thorough study of the electrical properties of Ni/h-BN/Ni tunneling devices based on epitaxial h-BN monolayer films. The electron tunneling is dominated by DT at lower biases, and the electrons flow only through an effective area, which is much smaller than the physical area of the device. At a higher voltage, the devices undergo a BD process. It is found that recoverable SBD with an extremely high compliance current of 100 mA dominates the failure behavior and can repeat up to 85 times before they are physically worn out, which indicates the extraordinary endurance of h-BN monolayers. The Weibull analysis of the BD voltages suggests that the BD paths are randomly distributed and the area-scaling law applies closely to the effective area rather than the physical area of the device. The minimum effective BD electric field is demonstrated to be 11.8 MV/cm, indicating high dielectric strength of the h-BN monolayers. Joule heat and electric field play important roles in the BD and recovery of devices.

■ ASSOCIATED CONTENT

Supporting Information

The Supporting Information is available free of charge at https://pubs.acs.org/doi/10.1021/acsaelm.9b00816.

https://dx.doi.org/10.1021/acsaelm.9b00816
ACS Appl. Electron. Mater. 2020, 2, 747−755

Growth conditions of h-BN monolayer samples; additional XPS analysis; structural and optical properties of additional samples; representative $I-V$ curves; and normalized Weibull plots from physical areas of the devices (PDF)

AUTHOR INFORMATION

Corresponding Author

Jianlin Liu − *Department of Electrical and Computer Engineering, University of California, Riverside, California 92521, United States;* orcid.org/0000-0001-6513-0867; Email: jianlin@ece.ucr.edu

Authors

Zhenjun Cui − *Department of Electrical and Computer Engineering, University of California, Riverside, California 92521, United States*

Yanwei He − *Department of Electrical and Computer Engineering, University of California, Riverside, California 92521, United States*

Hao Tian − *Department of Electrical and Computer Engineering, University of California, Riverside, California 92521, United States;* orcid.org/0000-0001-5893-2319

Alireza Khanaki − *Department of Electrical and Computer Engineering, University of California, Riverside, California 92521, United States*

Long Xu − *Department of Electrical and Computer Engineering, University of California, Riverside, California 92521, United States*

Wenhao Shi − *Department of Electrical and Computer Engineering, University of California, Riverside, California 92521, United States*

Complete contact information is available at: https://pubs.acs.org/10.1021/acsaelm.9b00816

Notes

The authors declare no competing financial interest.

ACKNOWLEDGMENTS

This work was supported by SHINES, an Energy Frontier Research Center funded by the US Department of Energy, Office of Science, Basic Energy Sciences under award #SC0012670.

REFERENCES

(1) Novoselov, K. S.; Jiang, D.; Schedin, F.; Booth, T. J.; Khotkevich, V. V.; Morozov, S. V.; Geim, A. K. Two-dimensional Atomic Crystals. *Proc. Natl. Acad. Sci. U.S.A.* **2005**, *102*, 10451−10453.

(2) Liu, Z.; Song, L.; Zhao, S.; Huang, J.; Ma, L.; Zhang, J.; Lou, J.; Ajayan, P. M. Direct Growth of Graphene/Hexagonal Boron Nitride Stacked Layers. *Nano Lett.* **2011**, *11*, 2032−2037.

(3) Suñé, J.; Placencia, I.; Barniol, N.; Farrés, E.; Martín, F.; Aymerich, X. On the Breakdown Statistics of Very Thin SiO_2 Films. *Thin Solid Films* **1990**, *185*, 347−362.

(4) Stathis, J. H. Percolation Models for Gate Oxide Breakdown. *J. Appl. Phys.* **1999**, *86*, 5757−5766.

(5) Obreja, V. V. N.; Codreanu, C.; Poenar, D.; Buiu, O. Edge Current Induced Failure of Semiconductor PN Junction During Operation in the Breakdown Region of Electrical Characteristic. *Microelectron. Reliab.* **2011**, *51*, 536−542.

(6) Uppal, H. J.; Mitrovic, I. Z.; Hall, S.; Hamilton, B.; Markevich, V.; Peaker, A. R. Breakdown and Degradation of Ultrathin Hf-based $(HfO_2)_x(SiO_2)_{1-x}$ Gate Oxide Films. *J. Vac. Sci. Technol. B* **2009**, *27*, 443−447.

(7) Ho, C.-H.; Kim, S. Y.; Roy, K. Ultra-Thin Dielectric Breakdown in Devices and Circuits: A Brief Review. *Microelectron. Reliab.* **2015**, *55*, 308−317.

(8) Watanabe, K.; Taniguchi, T.; Niiyama, T.; Miya, K.; Taniguchi, M. Far-Ultraviolet Plane-Emission Handheld Device Based on Hexagonal Boron Nitride. *Nat. Photonics* **2009**, *3*, 591.

(9) Kim, K. K.; Hsu, A.; Jia, X.; Kim, S. M.; Shi, Y.; Hofmann, M.; Nezich, D.; Rodriguez-Nieva, J. F.; Dresselhaus, M.; Palacios, T.; Kong, J. Synthesis of Monolayer Hexagonal Boron Nitride on Cu Foil Using Chemical Vapor Deposition. *Nano Lett.* **2011**, *12*, 161−166.

(10) Tay, R. Y.; Park, H. J.; Ryu, G. H.; Tan, D.; Tsang, S. H.; Li, H.; Liu, W.; Teo, E. H. T.; Lee, Z.; Lifshitz, Y.; Ruoff, R. S. Synthesis of Aligned Symmetrical Multifaceted Monolayer Hexagonal Boron Nitride Single Crystals on Resolidified Copper. *Nanoscale* **2016**, *8*, 2434−2444.

(11) Kidambi, P. R.; Blume, R.; Kling, J.; Wagner, J. B.; Baehtz, C.; Weatherup, R. S.; Schloegl, R.; Bayer, B. C.; Hofmann, S. In Situ Observations During Chemical Vapor Deposition of Hexagonal Boron Nitride on Polycrystalline Copper. *Chem. Mater.* **2014**, *26*, 6380−6392.

(12) Ismach, A.; Chou, H.; Mende, P.; Dolocan, A.; Addou, R.; Aloni, S.; Wallace, R.; Feenstra, R.; Ruoff, R. S.; Colombo, L. Carbon-Assisted Chemical Vapor Deposition of Hexagonal Boron Nitride. *2D Mater.* **2017**, *4*, 025117.

(13) Sutter, P.; Lahiri, J.; Zahl, P.; Wang, B.; Sutter, E. Scalable Synthesis of Uniform Few-Layer Hexagonal Boron Nitride Dielectric Films. *Nano Lett.* **2012**, *13*, 276−281.

(14) Gao, Y.; Ren, W.; Ma, T.; Liu, Z.; Zhang, Y.; Liu, W.-B.; Ma, L.-P.; Ma, X.; Cheng, H.-M. Repeated and Controlled Growth of Monolayer, Bilayer and Few-Layer Hexagonal Boron Nitride on Pt Foils. *ACS Nano* **2013**, *7*, 5199−5206.

(15) Kim, G.; Jang, A.-R.; Jeong, H. Y.; Lee, Z.; Kang, D. J.; Shin, H. S. Growth of High-Crystalline, Single-Layer Hexagonal Boron Nitride on Recyclable Platinum Foil. *Nano Lett.* **2013**, *13*, 1834−1839.

(16) Cun, H.; Hemmi, A.; Miniussi, E.; Bernard, C.; Probst, B.; Liu, K.; Alexander, D. T. L.; Kleibert, A.; Mette, G.; Weinl, M. Centimete-Sized Single-Orientation Monolayer Hexagonal Boron Nitride With or Without Nanovoids. *Nano Lett.* **2018**, *18*, 1205−1212.

(17) Park, J.-H.; Park, J. C.; Yun, S. J.; Kim, H.; Luong, D. H.; Kim, S. M.; Choi, S. H.; Yang, W.; Kong, J.; Kim, K. K.; Lee, Y. H. Large-Area Monolayer Hexagonal Boron Nitride on Pt Foil. *ACS Nano* **2014**, *8*, 8520−8528.

(18) Nakhaie, S.; Wofford, J. M.; Schumann, T.; Jahn, U.; Ramsteiner, M.; Hanke, M.; Lopes, J. M. J.; Riechert, H. Synthesis of Atomically Thin Hexagonal Boron Nitride Films on Nickel Foils by Molecular Beam Epitaxy. *Appl. Phys. Lett.* **2015**, *106*, 213108.

(19) Xu, Z.; Zheng, R.; Khanaki, A.; Zuo, Z.; Liu, J. Direct Growth of Graphene on In Situ Epitaxial Hexagonal Boron Nitride Flakes by Plasma-Assisted Molecular Beam Epitaxy. *Appl. Phys. Lett.* **2015**, *107*, 213103.

(20) Zuo, Z.; Xu, Z.; Zheng, R.; Khanaki, A.; Zheng, J. G.; Liu, J. In-situ epitaxial growth of graphene/h-BN van der Waals heterostructures by molecular beam epitaxy. *Sci. Rep.* **2015**, *5*, 14760.

(21) Xu, Z.; Khanaki, A.; Tian, H.; Zheng, R.; Suja, M.; Zheng, J.-G.; Liu, J. Direct growth of hexagonal boron nitride/graphene heterostructures on cobalt foil substrates by plasma-assisted molecular beam epitaxy. *Appl. Phys. Lett.* **2016**, *109*, 043110.

(22) Khanaki, A.; Tian, H.; Xu, Z.; Zheng, R.; He, Y.; Cui, Z.; Yang, J.; Liu, J. Effect of High Carbon Incorporation in Co Substrates on the Epitaxy of Hexagonal Boron Nitride/Graphene Heterostructures. *Nanotechnology* **2017**, *29*, 035602.

(23) Xu, Z.; Tian, H.; Khanaki, A.; Zheng, R.; Suja, M.; Liu, J. Large-area Growth of Multi-Layer Hexagonal Boron Nitride on Polished Cobalt Foils by Plasma-Assisted Molecular Beam Epitaxy. *Sci. Rep.* **2017**, *7*, 43100.

(24) Tian, H.; Khanaki, A.; Das, P.; Zheng, R.; Cui, Z.; He, Y.; Shi, W.; Xu, Z.; Lake, R.; Liu, J. Role of Carbon Interstitials in Transition Metal Substrates on Controllable Synthesis of High-Quality Large-

Area Two-Dimensional Hexagonal Boron Nitride Layers. *Nano Lett.* **2018**, *18*, 3352−3361.
(25) He, Y.; Tian, H.; Khanaki, A.; Shi, W.; Tran, J.; Cui, Z.; Wei, P.; Liu, J. Large-Area Adlayer-Free Single-Layer h-BN Film Achieved by Controlling Intercalation Growth. *Appl. Surf. Sci.* **2019**, *498*, 143851.
(26) Tonkikh, A.; Voloshina, E.; Werner, P.; Blumtritt, H.; Senkovskiy, B.; Güntherodt, G.; Parkin, S.; Dedkov, Y. S. Structural and Electronic Properties of Epitaxial Multilayer h-BN on Ni (111) for Spintronics Applications. *Sci. Rep.* **2016**, *6*, 23547.
(27) Meng, J.; Zhang, X.; Wang, Y.; Yin, Z.; Liu, H.; Xia, J.; Wang, H.; You, J.; Jin, P.; Wang, D.; Meng, X.-M. Aligned Growth of Millimeter-Size Hexagonal Boron Nitride Single-Crystal Domains on Epitaxial Nickel Thin Film. *Small* **2017**, *13*, 1604179.
(28) Wang, H.; Zhang, X.; Meng, J.; Yin, Z.; Liu, X.; Zhao, Y.; Zhang, L. Controlled Growth of Few-Layer Hexagonal Boron Nitride on Copper Foils Using Ion Beam Sputtering Deposition. *Small* **2015**, *11*, 1542−1547.
(29) Britnell, L.; Gorbachev, R. V.; Jalil, R.; Belle, B. D.; Schedin, F.; Katsnelson, M. I.; Eaves, L.; Morozov, S. V.; Mayorov, A. S.; Peres, N. M. Tunneling Through Ultrathin Boron Nitride Crystalline Barriers. *Nano Lett.* **2012**, *12*, 1707−1710.
(30) Lee, G.-H.; Yu, Y.-J.; Lee, C.; Dean, C.; Shepard, K. L.; Kim, P.; Hone, J. Electron Tunneling Through Atomically Flat and Ultrathin Hexagonal Boron Nitride. *Appl. Phys. Lett.* **2011**, *99*, 243114.
(31) Hattori, Y.; Taniguchi, T.; Watanabe, K.; Nagashio, K. Layer-By-Layer Dielectric Breakdown of Hexagonal Boron Nitride. *ACS Nano* **2014**, *9*, 916−921.
(32) Jiang, L.; Shi, Y.; Hui, F.; Tang, K.; Wu, Q.; Pan, C.; Jing, X.; Uppal, H.; Palumbo, F.; Lu, G. Breakdown in Chemical Vapor Deposited Hexagonal Boron Nitride. *ACS Appl. Mater. Interfaces* **2017**, *9*, 39758−39770.
(33) Ranjan, A.; Raghavan, N.; Puglisi, F. M.; Mei, S.; Padovani, A.; Larcher, L.; Shubhakar, K.; Pavan, P.; Bosman, M.; Zhang, X. X.; O'Shea, S. J.; Pey, K. L. Boron Vacancies Causing Breakdown in 2D Layered Hexagonal Boron Nitride Dielectrics. *IEEE Electron Device Lett.* **2019**, *40*, 1321−1324.
(34) Hwan Lee, S.; Sup Choi, M.; Lee, J.; Ho Ra, C.; Liu, X.; Hwang, E.; Hee Choi, J.; Zhong, J.; Chen, W.; Jong Yoo, W. High Performance Vertical Tunneling Diodes Using Graphene/Hexagonal Boron Nitride/Graphene Hetero-Structure. *Appl. Phys. Lett.* **2014**, *104*, 053103.
(35) Guo, N.; Wei, J.; Jia, Y.; Sun, H.; Wang, Y.; Zhao, K.; Shi, X.; Zhang, L.; Li, X.; Cao, A.; Zhu, H.; Wang, K.; Wu, D. Fabrication of Large Area Hexagonal Boron Nitride Thin Films for Bendable Capacitors. *Nano Res.* **2013**, *6*, 602−610.
(36) Hattori, Y.; Taniguchi, T.; Watanabe, K.; Nagashio, K. Determination of Carrier Polarity in Fowler−Nordheim Tunneling and Evidence of Fermi Level Pinning at the Hexagonal Boron Nitride/Metal Interface. *ACS Appl. Mater. Interfaces* **2018**, *10*, 11732−11738.
(37) Sutter, P.; Lahiri, J.; Zahl, P.; Wang, B.; Sutter, E. Scalable Synthesis of Uniform Few-Layer Hexagonal Boron Nitride Dielectric Films. *Nano Lett.* **2012**, *13*, 276−281.
(38) Hattori, Y.; Taniguchi, T.; Watanabe, K.; Nagashio, K. Anisotropic Dielectric Breakdown Strength of Single Crystal Hexagonal Boron Nitride. *ACS Appl. Mater. Interfaces* **2016**, *8*, 27877−27884.
(39) Tian, H.; He, Y.; Das, P.; Cui, Z.; Shi, W.; Khanaki, A.; Lake, R. K.; Liu, J. Growth Dynamics of Millimeter-Sized Single-Crystal Hexagonal Boron Nitride Monolayers on Secondary Recrystallized Ni (100) Substrates. *Adv. Mater. Interfaces* **2019**, *6*, 1901198.
(40) Khan, M. H.; Huang, Z.; Xiao, F.; Casillas, G.; Chen, Z.; Molino, P. J.; Liu, H. K. Synthesis of Large and Few Atomic Layers of Hexagonal Boron Nitride on Melted Copper. *Sci. Rep.* **2015**, *5*, 7743.
(41) Arenal, R.; Ferrari, A. C.; Reich, S.; Wirtz, L.; Mevellec, J.-Y.; Lefrant, S.; Rubio, A.; Loiseau, A. Raman Spectroscopy of Single-Wall Boron Nitride Nanotubes. *Nano Lett.* **2006**, *6*, 1812−1816.
(42) Elias, C.; Valvin, P.; Pelini, T.; Summerfield, A.; Mellor, C.; Cheng, T.; Eaves, L.; Foxon, C.; Beton, P.; Novikov, S. Direct Band-Gap Crossover in Epitaxial Monolayer Boron Nitride. *Nat. Commun.* **2019**, *10*, 2639.
(43) Caneva, S.; Weatherup, R. S.; Bayer, B. C.; Blume, R.; Cabrero-Vilatela, A.; Braeuninger-Weimer, P.; Martin, M.-B.; Wang, R.; Baehtz, C.; Schloegl, R.; Meyer, J. C.; Hofmann, S. Controlling Catalyst Bulk Reservoir Effects for Monolayer Hexagonal Boron Nitride CVD. *Nano Lett.* **2016**, *16*, 1250−1261.
(44) Schwarz, M.; Riss, A.; Garnica, M.; Ducke, J.; Deimel, P. S.; Duncan, D. A.; Thakur, P. K.; Lee, T.-L.; Seitsonen, A. P.; Barth, J. V.; Allegretti, F.; Auwärter, W. Corrugation in the Weakly Interacting Hexagonal-BN/Cu (111) System: Structure Determination by Combining Noncontact Atomic Force Microscopy and X-Ray Standing Waves. *ACS Nano* **2017**, *11*, 9151−9161.
(45) Simmons, J. G. Generalized Formula for the Electric Tunnel Effect Between Similar Electrodes Separated by a Thin Insulating Film. *J. Appl. Phys.* **1963**, *34*, 1793−1803.
(46) Simmons, J. G. Generalized Thermal J-V Characteristic for the Electric Tunnel Effect. *J. Appl. Phys.* **1964**, *35*, 2655−2658.
(47) Raghavan, N.; Pey, K. L.; Shubhakar, K. High-κ Dielectric Breakdown in Nanoscale Logic Devices−Scientific Insight and Technology Impact. *Microelectron. Reliab.* **2014**, *54*, 847−860.
(48) Ge, R.; Wu, X.; Kim, M.; Chou, H.; Sonde, S.; Tao, L.; Lee, J. C.; Akinwande, D. Towards Universal Non-Volatile Resistance Switching in Non-metallic Monolayer Atomic Sheets. **2017**, arXiv:1709.04592. arXiv preprint.
(49) Jang, S. K.; Youn, J.; Song, Y. J.; Lee, S. Synthesis and Characterization of Hexagonal Boron Nitride as a Gate Dielectric. *Sci. Rep.* **2016**, *6*, 30449.
(50) Xu, Y.-N.; Ching, W. Y. Calculation of Ground-State and Optical Properties of Boron Nitrides in the Hexagonal, Cubic, and Wurtzite Structures. *Phys. Rev. B: Condens. Matter Mater. Phys.* **1991**, *44*, 7787.
(51) Dorneles, L. S.; Schaefer, D. M.; Carara, M.; Schelp, L. F. The Use of Simmons' Equation to Quantify the Insulating Barrier Parameters in Al/AlO_x/Al Tunnel Junctions. *Appl. Phys. Lett.* **2003**, *82*, 2832−2834.
(52) Åkerman, J. J.; Slaughter, J. M.; Dave, R. W.; Schuller, I. K. Tunneling Criteria for Magnetic-Insulator-Magnetic Structures. *Appl. Phys. Lett.* **2001**, *79*, 3104−3106.
(53) Dodson, B. *Weibull Analysis*; Asq Press, 1994.
(54) Wu, E. Y.; Vollertsen, R.-P. On the Weibull Shape Factor of Intrinsic Breakdown of Dielectric Films and Its Accurate Experimental Determination. Part I: Theory, Methodology, Experimental Techniques. *IEEE Trans. Electron Devices* **2002**, *49*, 2131−2140.
(55) Schlitz, R. A.; Yoon, K.; Fredin, L. A.; Ha, Y.-g.; Ratner, M. A.; Marks, T. J.; Lauhon, L. J. Weibull Analysis of Dielectric Breakdown in a Self-Assembled Nanodielectric for Organic Transistors. *J. Phys. Chem. Lett.* **2010**, *1*, 3292−3297.
(56) Wu, E. Y.; Li, B.; Stathis, J. H. Modeling of Time-Dependent Non-Uniform Dielectric Breakdown Using a Clustering Statistical Approach. *Appl. Phys. Lett.* **2013**, *103*, 152907.
(57) Pompl, T.; Engel, C.; Wurzer, H.; Kerber, M. Soft Breakdown and Hard Breakdown in Ultra-Thin Oxides. *Microelectron. Reliab.* **2001**, *41*, 543−551.
(58) Takagi, S.-i.; Takayanagi, M. Carrier Transport Properties of Thin Gate Oxides After Soft and Hard Breakdown. *Microelectron. Eng.* **2001**, *59*, 5−15.
(59) Wang, P.; Perini, C. J.; O'Hara, A.; Gong, H.; Wang, P.; Zhang, E. X.; McCurdy, M. W.; Fleetwood, D. M.; Schrimpf, R. D.; Pantelides, S. T.; Vogel, E. M. Total Ionizing Dose Effects and Proton-Induced Displacement Damage on MoS2-Interlayer-MoS2 Tunneling Junctions. *IEEE Trans. Nucl. Sci.* **2019**, *66*, 420−427.
(60) Kotakoski, J.; Jin, C. H.; Lehtinen, O.; Suenaga, K.; Krasheninnikov, A. V. Electron knock-on damage in hexagonal boron nitride monolayers. *Phys. Rev. B: Condens. Matter Mater. Phys.* **2010**, *82*, 113404.
(61) Weston, L.; Wickramaratne, D.; Mackoit, M.; Alkauskas, A.; Van de Walle, C. G. Native point defects and impurities in hexagonal boron nitride. *Phys. Rev. B* **2018**, *97*, 214104.

https://dx.doi.org/10.1021/acsaelm.9b00816
ACS Appl. Electron. Mater. 2020, 2, 747−755

(62) Cai, Q.; Scullion, D.; Gan, W.; Falin, A.; Zhang, S.; Watanabe, K.; Taniguchi, T.; Chen, Y.; Santos, E. J. G.; Li, L. H. High Thermal Conductivity of High-Quality Monolayer Boron Nitride and Its Thermal Expansion. *Sci. Adv.* **2019**, *5*, No. eaav0129.
(63) Gu, X.; Yang, R. Phonon Transport and Thermal Conductivity in Two-Dimensional Materials. *Annu. Rev. Heat Transfer* **2016**, *19*, 1−65.
(64) Suñé, J.; Nafría, M.; Aymerich, X. Reversible Dielectric Breakdown of Thin Gate Oxides in MOS Devices. *Microelectron. Reliab.* **1993**, *33*, 1031−1039.

https://dx.doi.org/10.1021/acsaelm.9b00816
ACS Appl. Electron. Mater. 2020, 2, 747−755